Neurobiology of Disease

# Medial Temporal Lobe Networks in Alzheimer's Disease: Structural and Molecular Vulnerabilities

**Robin de Flores,[1,2] Sandhitsu R. Das,[3] Long Xie,[3,4] Laura E. M. Wisse,[3,5] Xueying Lyu,[6] Preya Shah,[6] Paul A. Yushkevich,[3] and David A. Wolk[1]**

[1]Department of Neurology, University of Pennsylvania, Philadelphia 19104, Pennsylvania, [2]Université de Caen Normandie, Institut National de la Santé et de la Recherche Médicale Unité Mixte de Recherche Scientifique (UMRS) Unité 1237, Caen 14000, France, [3]Penn Image Computing and Science Laboratory (PICSL), University of Pennsylvania, Philadelphia 19104, Pennsylvania, [4]Department of Radiology, University of Pennsylvania, Philadelphia 19104, Pennsylvania, [5]Department of Diagnostic Radiology, Lund University, Lund 22185, Sweden, and [6]Department of Bioengineering, University of Pennsylvania, Philadelphia 19104, Pennsylvania

**The medial temporal lobe (MTL) is connected to the rest of the brain through two main networks: the anterior-temporal (AT) and the posterior-medial (PM) systems. Given the crucial role of the MTL and networks in the physiopathology of Alzheimer's disease (AD), the present study aimed at (1) investigating whether MTL atrophy propagates specifically within the AT and PM networks, and (2) evaluating the vulnerability of these networks to AD proteinopathies. To do that, we used neuroimaging data acquired in human male and female in three distinct cohorts: (1) resting-state functional MRI (rs-fMRI) from the aging brain cohort (ABC) to define the AT and PM networks ($n = 68$); (2) longitudinal structural MRI from Alzheimer's disease neuroimaging initiative (ADNI)GO/2 to highlight structural covariance patterns ($n = 349$); and (3) positron emission tomography (PET) data from ADNI3 to evaluate the networks' vulnerability to amyloid and tau ($n = 186$). Our results suggest that the atrophy of distinct MTL subregions propagates within the AT and PM networks in a dissociable manner. Brodmann area (BA)35 structurally covaried within the AT network while the parahippocampal cortex (PHC) covaried within the PM network. In addition, these networks are differentially associated with relative tau and amyloid burden, with higher tau levels in AT than in PM and higher amyloid levels in PM than in AT. Our results also suggest differences in the relative burden of tau species. The current results provide further support for the notion that two distinct MTL networks display differential alterations in the context of AD. These findings have important implications for disease spread and the cognitive manifestations of AD.**

*Key words:* **Alzheimer's disease; medial temporal lobe; networks; neurodegeneration; proteinopathies**

**Significance Statement**

**The current study provides further support for the notion that two distinct medial temporal lobe (MTL) networks, i.e., anterior-temporal (AT) and the posterior-medial (PM), display differential alterations in the context of Alzheimer's disease (AD). Importantly, neurodegeneration appears to occur within these networks in a dissociable manner marked by their covariance patterns. In addition, the AT and PM networks are also differentially associated with relative tau and amyloid burden, and perhaps differences in the relative burden of tau species [e.g., neurofibriliary tangles (NFTs) vs tau in neuritic plaques]. These findings, in the context of a growing literature consistent with the present results, have important implications for disease spread and the cognitive manifestations of AD in light of the differential cognitive processes ascribed to them.**

Received May 3, 2021; revised Nov. 30, 2021; accepted Dec. 4, 2021.

Author contributions: R.d.F. and D.A.W. designed research; R.d.F., S.R.D., L.X., L.E.M.W., X.L., P.S., and P.A.Y. analyzed data; R.d.F., S.R.D., L.X., L.E.M.W., X.L., P.S., P.A.Y., and D.A.W. performed research; R.d.F. wrote the first draft of the paper; R.d.F., S.R.D., L.X., L.E.M.W., P.S., P.A.Y., and D.A.W. edited the paper; R.d.F. and D.A.W. wrote the paper.

This work was supported by National Institutes of Health Grants AG10124, AG056014, and EB017255; the Alzheimer's Association Grant AARF-19-615258; MultiPark - A Strategic Research Area at Lund University and the Fondation Philippe Chatrier. Data used in preparation of this article were obtained from the ADNI database (http://adni.loni.usc.edu/). As such, the investigators within the ADNI contributed to the design and implementation of ADNI and/or provided data but did not participate in analysis or writing of this report. A complete listing of ADNI investigators can be found at http://adni.loni.usc.edu/wp-content/uploads/how_to_apply/ADNI_Acknowledgement_List.pdf.

D.A.W. receives grant support from Avid Radiopharmaceuticals/Eli Lilly, Biogen, Functional Neuromodulation, and Merck. L.X. received personal consulting fees from Galileo CDS, Inc. All other authors declare no competing financial interests.

Correspondence should be addressed to Robin de Flores at deflores@cyceron.fr.

https://doi.org/10.1523/JNEUROSCI.0949-21.2021



## Introduction

The medial temporal lobe (MTL) is the earliest region to display atrophy over the course of Alzheimer's disease (AD), consistent with early neurofibriliary tangle (NFT) involvement. This is followed by spread of NFTs and concomitant atrophy, in a stereotypical manner, reaching limbic regions and ultimately the neocortex (Braak and Braak, 1991; Pini et al., 2016). This topographical overlap suggests a direct relationship between tau pathology and atrophy, which has been confirmed in studies associating structural MRI with pathology (Whitwell et al., 2008; de Flores et al., 2020), CSF (de Souza et al., 2012; Tardif et al., 2018), or positron emission tomography (PET; Das et al., 2018;

Xie et al., 2018; La Joie et al., 2020) measures of tau pathology. Importantly, tau pathology and subsequent atrophy spread across anatomically interconnected regions, which has led to the theory of a "prion-like" propagation, where pathology spreads within specific networks (Peng et al., 2020). Recent imaging investigations support this idea, showing a close relationship between functional connectivity and tau/neurodegeneration topography and propagation (Seeley et al., 2009; Ossenkoppele et al., 2019; Franzmeier et al., 2020a,b).

The MTL is composed of several subregions including the hippocampus as well as entorhinal cortex (ERC), perirhinal cortex [PRC; including Brodmann areas (BA)35 and BA36], and parahippocampal cortex (PHC). These different regions do not function in isolation but are connected to the rest of the brain through two specific networks that converge in the hippocampus. The anterior-temporal (AT) network, composed of the PRC, anterior hippocampus (aH), lateral ERC, amygdala, and temporopolar and lateral orbitofrontal cortices, is thought to support object and semantic memory, object perception and affective/emotion processing. The posterior-medial (PM) network, composed of PHC, posterior hippocampus (pH), medial ERC, retrosplenial cortex, precuneus, angular gyrus, and medial prefrontal cortex, is preferentially involved in episodic memory, scene perception and social cognition (Ranganath and Ritchey, 2012). Importantly, available data from the literature have demonstrated a functional vulnerability of these specific systems in the context of normal aging and early AD. However, findings are partly inconsistent, showing reduced connectivity within the PM network and either reduced or increased AT network connectivity (Das et al., 2015; Liu et al., 2016; Salami et al., 2016; Berron et al., 2020). In addition, recent publications suggest a specific sensitivity of the AT and PM systems to AD pathology, where tau preferentially deposits in the AT network while amyloid pathology was preferentially found in PM regions (Adams et al., 2019; Maass et al., 2019).

Given the crucial role of the MTL and brain networks in the physiopathology of AD, the present study aimed at investigating the structural and molecular vulnerabilities of the AT and PM systems over the course of the disease. To do that, we used a combination of resting-state functional MRI (rs-fMRI), longitudinal structural MRI as well as tau and amyloid PET data acquired in three distinct cohorts covering the full AD spectrum. In particular, we wanted to determine whether longitudinal atrophy occurred conjointly within or across these networks. If the former, this would support the notion of neurodegeneration occurring along networks, potentially because of transsynaptic spread of pathology. To address this, we evaluated whether longitudinal atrophy in BA35 and PHC, two MTL nodes of the AT versus PM systems, respectively, structurally covaried with distinct brain regions reflecting the AT versus PM networks, which were defined with resting state functional connectivity data from an independent older adult cohort. In addition, we aimed to further our understanding regarding the relative vulnerability of these two systems to amyloid and tau pathologies. Based on prior observations, we hypothesized that tau-PET uptake was relatively higher in the AT network while amyloid uptake was higher in the PM network. To go further, we investigated whether the relationship between both pathologies is different within the AT and PM networks.

## Materials and Methods

### Participants

*Alzheimer's disease neuroimaging initiative (ADNI)*

Part of the data used in the preparation of this article was obtained from the ADNI database (https://adni.loni.usc.edu/). The ADNI was launched in 2003 as a public–private partnership, led by Principal Investigator Michael W. Weiner. The primary goal of ADNI has been to test whether serial MRI, PET, other biological markers, and clinical and neuropsychological assessment can be combined to measure the progression of MCI and early AD. For up-to-date information, see www.adni-info.org.

Participants in ADNI GO and ADNI 2 studies who had longitudinal T1-weighted (T1w) MRI scans and $\beta$-amyloid PET scans available were considered for this study. All available scans within 1.2- to 2.5-year follow-up were analyzed for each participant. A summary standardized uptake value ratio (SUVR) derived from Florbetapir PET (available publicly in the processed data on the ADNI website) was used to determine the A$\beta$ status of each participant by applying a threshold of SUVR $\geq$ 1.11 (Landau et al., 2013). In total, 349 participants were selected and grouped into A$\beta$ negative (A$\beta-$) cognitively normal (CN) controls, A$\beta$ positive (A$\beta+$) CN, A$\beta+$ mild cognitive impairment (MCI), and A$\beta+$ AD patients.

Participants in ADNI 3 with available $\beta$-amyloid and tau PET scans were also included in this study. As described previously, a threshold of SUVR $\geq$ 1.11 was used to determine the A$\beta$ status. In total, 186 participants were selected and grouped into A$\beta$ + CN, A$\beta+$ MCI, and A$\beta+$ AD patients.

*Aging brain cohort (ABC)*

CN older adults enrolled in the ABC who had T1w and resting-state fMRI scans available were considered for this study. These participants were recruited from the Clinical Core of the Alzheimer's Disease Core Center (ADCC) at the University of Pennsylvania. These individuals are evaluated on an annual basis, including standard psychometric testing as prescribed by the Uniform Data Set 3.0 (UDS 3.0; Weintraub et al., 2018) and given an annual consensus diagnostic designation. This study was approved by the Institutional Review Board of the University of Pennsylvania and informed consent was provided by all subjects. In total, 68 CN participants were selected.

The demographic characteristics of the samples are summarized in Table 1. See Figure 1 for flow-charts showing the process of arriving at these cohorts.

### Neuroimaging data acquisition

*ADNI imaging protocol*

The MRI imaging protocols of the ADNI study that were used to acquire the T1w MRI scans were previously described in Jack et al. (2008) and Leow et al. (2006). Amyloid PET imaging consisted of a continuous 200min brain scan (four frames of 5-min duration) 50 min following ~10 mCi of $^{18}$F-florbetapir injection. Tau PET imaging consisted of a continuous 30-min brain scan (six frames of 5-min duration) 75 min following ~10 mCi of $^{18}$F-flortaucipir injection. Amyloid and tau PET images were downloaded from the ADNI data archive in the most fully postprocessed format with the image description "Coreg, Avg, Std Img and Vox Siz, Uniform Resolution." Up-to-date information about ADNI imaging protocols can be found at adni.loni.usc.edu/methods/mri-tool/mri-analysis and http://adni.loni.usc.edu/methods/pet-analysis-method/pet-analysis.

*ABC imaging protocol*

Each subject of the ABC underwent a MR scan at the University of Pennsylvania using a 3T Siemens MAGNETOM Prisma MRI scanner. First, T1w structural images were acquired [repetition time (TR) = 2400 ms; echo time (TE) = 2.24 ms; inversion time (TI) = 1060 ms; flip angle = 8°; 208 axial slices; slice thickness = 0.8 mm; field of view = 240 × 256 mm$^2$; matrix = 300 × 320; in-plane resolution = 0.8 × 0.8 mm$^2$; acquisition time = 6.38 min]. Second, resting-state functional acquisitions were obtained using a gradient-echo echoplanar (EPI) sequence (TR = 720 ms; TE = 37 ms; flip angle = 52°; 72 axial slices; slice thickness = 2 mm; field of view = 208 × 208 mm$^2$; matrix = 104 × 104; in-plane resolution = 2 × 2 mm$^2$; multiband acceleration factor = 8; 420 volumes; acquisition time = 5.12 min). Finally, B0 maps were acquired (TR = 580 ms; TE1 = 4.12 ms; TE2 = 6.58 ms; flip angle = 45°; 60 axial slices; slice thickness = 3 mm; field of view = 240 × 240 mm$^2$; matrix = 80 × 80; in-plane resolution = 3 × 3 mm$^2$; acquisition time = 1.34 min).

**Table 1. Demographics of the samples**

| Structural covariance analyses: ADNI GO and ADNI 2 | | | | |
|---|---|---|---|---|
| | CN A$\beta-$ ($n = 117$) | CN A$\beta+$ ($n = 65$) | MCI A$\beta+$ ($n = 148$) | AD A$\beta+$ ($n = 19$) |
| Age (SD), year | 71.9 (6.1) | 75.3 (5.8) | 72.9 (6.6) | 75.6 (8.7) |
| Sex (F, M) | 57,60 | 43,22 | 65,83 | 11,8 |
| Education (SD), year | 17.1 (2.3) | 16.0 (2.8) | 16.3 (2.7) | 15.9 (2.7) |
| MMSE | 29.1 (1.3) | 29.1 (0.9) | 27.7 (1.8) | 22.7 (9.7) |
| Number of scans (SD) | 2.4 (0.5) | 2.4 (0.5) | 2.5 (0.5) | 2.3 (0.5) |
| Follow-up time (SD), d | 655.6 (174.5) | 669.8 (164.3) | 602.0 (186.3) | 540.2 (167.6) |
| PET analyses: ADNI 3 | | | | |
| | CN A$\beta+$ ($n = 67$) | MCI A$\beta+$ ($n = 71$) | AD A$\beta+$ ($n = 48$) | |
| Age (SD), year | 76.9 (5.8) | 76.2 (6.8) | 78.0 (9.3) | |
| Sex (F, M) | 23,44 | 40,31 | 25,23 | |
| Education (SD), year | 16.5 (2.3) | 15.8 (2.6) | 15.3 (2.4) | |
| MMSE (SD) | 28.7 (1.6) | 26.9 (2.2) | 22.1 (4.4) | |
| Functional connectivity analyses: ABC | | | | |
| | CN ($n = 68$) | | | |
| Age (SD), year | 71.6 (6.5) | | | |
| Sex (F, M) | 44,24 | | | |
| Education (SD), year | 15.8 (2.6) | | | |
| MMSE (SD) | 29.2 (0.9) | | | |

CN, cognitively normal; MCI, mild cognitive impairment; A$\beta$, amyloid-$\beta$; MMSE, Mini-Mental State Examination.

## Image processing

*Longitudinal structural measures of MTL subregions (ADNI GO/2)*

The longitudinal MRI scans from ADNI were processed using a tailored pipeline that accounts for common confounds of conventional approaches. A multiatlas automatic segmentation algorithm "ASHS-T1" (Xie et al., 2019, 2020; de Flores et al., 2020) was used to label the anterior and pH, ERC, PRC (subdivided in BA35 and BA36), and PHC in each baseline MRI scan. The relative annualized volume atrophy rate (in %) was computed for each region using a deformation-based morphometry pipeline and a comprehensive quality control was performed as described in a previous publication (Xie et al., 2020). More precisely, the quality control included three levels: the MRI scans, the ASHS-T1 automatic segmentation, and the longitudinal estimation. In the first step, all the baseline MRI scans were checked visually and those with severe motion artifact or blurring were excluded. Then, baseline ASHS-T1 segmentations were visually checked for all subjects. All subjects included in the present study had good quality segmentations for BA35 and PHC, as these regions are of specific interest in our analyses. Lastly, the quality of longitudinal estimation was assessed. Scans of follow-up timepoints that were poorly registered to the baseline were excluded from the atrophy rate estimation. However, because of the very large number of registration pairs, it was not feasible to visually check all of them. Instead, we checked a subset of registrations selected using the following method: (1) we computed the normalized cross-correlation (NCC) of the registered scans, which is a good indicator of registration quality, and then selected pairs of registrations that yielded NCC that are 1.5 SD below the mean. (2) We also randomly selected 5% of the remaining pairs to confirm that they had high registration quality. Bilateral measurements of each subregion were averaged.

*Whole-brain longitudinal mapping of cortical thickness (ADNI GO/2)*

The ANTs longitudinal cortical thickness pipeline was used to generate whole brain atrophy maps (Tustison et al., 2019). First, a group template and corresponding prior probability images were created using an independent group of 52 CN ADNI-1 subjects, as previously described (Tustison et al., 2019). Then, an unbiased single-subject template (SST) was created for each subject of the present study. The ANTs cross-sectional cortical thickness pipeline (Tustison et al., 2014) was applied to the SST (with the group template and priors as input). SST prior probability maps were created and the ANTs cross-sectional cortical thickness pipeline, with the SST as the reference template, was applied to each individual time point image. Least squares regression models were applied to estimate annualized change based on each time point cortical thickness maps for each subject. Each resulting whole brain atrophy maps, warped to the template space, was visually checked and no failure was detected.

*rs-fMRI (ABC)*

First, data were checked for the lack of artifact or of abnormal variance distribution through the application of the TSDiffana routine (https://imaging.mrc-cbu.cam.ac.uk/imaging/DataDiagnostics). B0 maps were then used to perform susceptibility distortion correction. Next, six-parameter rigid body motion correction was implemented to account for head motion-related artifacts (Friston et al., 1995). All included subjects experienced minimal head motion (<2-mm translation and <2° rotation in any direction) at all times during acquisition. Following motion correction, the fMRI data were co-registered to the T1 structural scan. A 4-mm full-width at half-maximal (FWHM) smoothing was applied to the rs-fMRI scan together with a bandpass filter (0.008–0.08 Hz) to the time series to reduce low-frequency drift and high-frequency noise. Physiologic noise was eliminated via linear regression to factor out the global signal and mean signals from white matter and CSF regions. The Atropos method was used for three-tissue segmentation (Avants et al., 2011). We also regressed out the six parameters of head motion (obtained from motion correction) and their six temporal derivatives to minimize motion-induced signal variation.

Anatomical regions from ASHS-T1 segmentations were used as regions of interest (ROIs). More precisely, the union of the aH and BA35 was used as the seed region for the AT system, and the union of the pH and PHC was used as the seed for the PM system, in accordance to Ranganath and Ritchey (2012). Segmentations were carefully visually checked manually edited when needed. Note that the ERC was not used as a seed since this region is thought be involved in both the AT and PM systems (Maass et al., 2015). Since time series were extracted after a 4 mm smoothing, several slices perpendicular to the long axis of the hippocampus were removed from the aH and pH ROIs to avoid signal contamination from one ROI to the other (see Fig. 2). In order to remove these voxels, an intermediate step was necessary. High-resolution T2 images ($0.4 \times 0.4 \times 1.2$ mm$^3$) acquired perpendicular to the long axis of the hippocampus were available for each subject. aH and pH were first transformed to T2 space. Then, the two most posterior slices of the aH ROI and the three most anterior slices of the pH ROI were isolated to generate a 6-mm exclusion mask. This mask was transformed to T1 space and each voxel were removed from the original aH and pH ROIs.

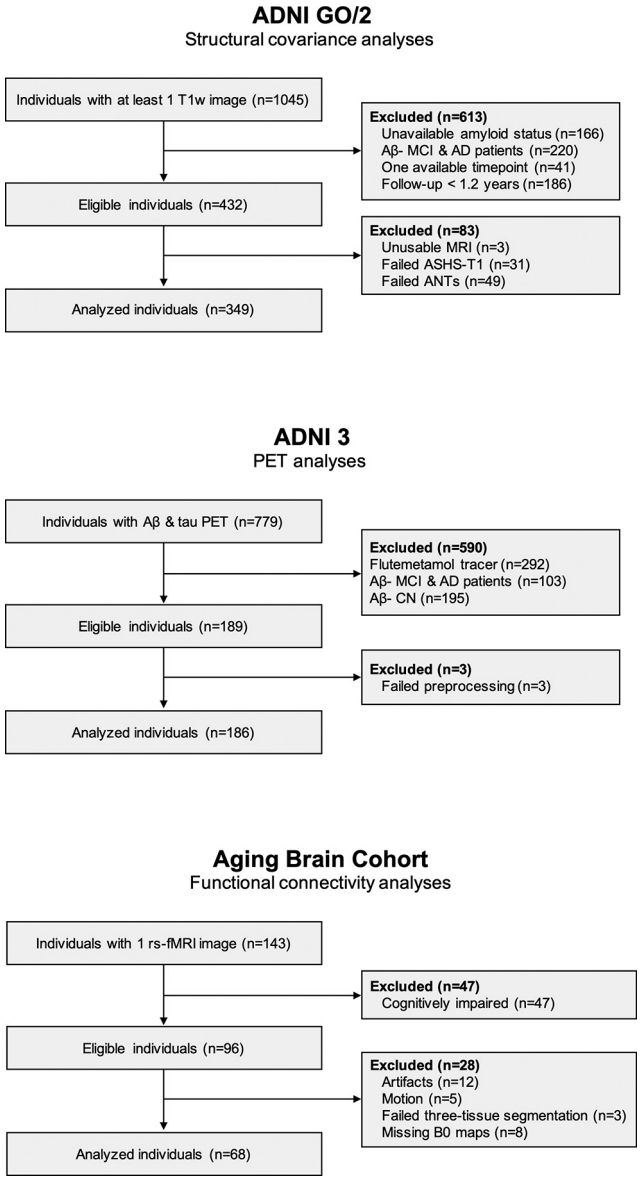


**Figure 1.** Flow-charts showing cohorts selection.

Thus, the ROIs were not adjacent and signal from one ROI was unlikely to contaminate the other. Linear Pearson correlations between the average residual time-series signals for each seed were used to generate functional connectivity maps for each subject (two maps per subject). The resulting connectivity maps were Fisher r-z transformed for variance stabilization, warped to template space and a 6-mm FWHM smoothing was applied. Unsmoothed warped connectivity maps were also averaged across all subjects, resulting in an average connectivity map for each of the two seeds.

*Amyloid and Tau PET (ADNI 3)*

The postprocessed $^{18}$F-florbetapir and $^{18}$F-flortaucipir PET images were generated by averaging coregistered individual frames, re-oriented in a standardized image space such that the anterior-posterior axis of the subject is parallel to the AC-PC line, followed by scanner-specific filtering to generate an image with a uniform isotropic resolution of 8 mm full width half maximum. More details about the preprocessing used is described at http://adni.loni.usc.edu/methods/pet-analysis-method/pet-analysis/. Postprocessed PET images were then registered to subject's T1w structural MRI using ANTs. The MRI scan was parcellated into cerebellar, cortical, and subcortical ROIs using a multiatlas segmentation method (Wang et al., 2011). The atlas set and the resulting segments are

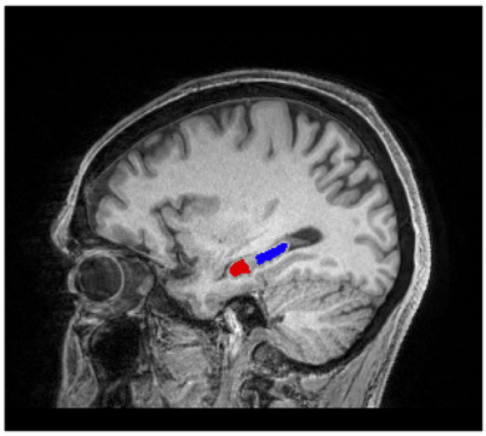

**Figure 2.** Example of ASHS-T1 hippocampal ROIs used as seeds for functional connectivity analyses. A 6-mm gap was generated between the two ROIs to avoid signal contamination from one ROI to the other. Red, aH; blue, pH.

described in the study by Landman and Warfield (2012). Mean PET tracer uptake in the cerebellar gray matter and gray+white matter was used as reference regions for $^{18}$F-Flortaucipir and $^{18}$F-Florbetapir, respectively, and a SUVR map was generated for each participant for each PET modality. Each SUVR map was then moved to template space using ANTs and masked to only include gray matter voxels. Since amyloid and tau co-localize into neuritic plaques, a subset of amyloid plaques defined by the presence of hyperphosphorylated tau protein (Jellinger, 2020), we generated tau to amyloid ratio (tau/amyloid) maps to better highlight tau pathology that may be relatively more or less independent of amyloid pathology. To do that, the warped SUVR tau map was divided by the warped SUVR amyloid map (at the voxel level) for each subject. Tau, amyloid and tau/amyloid scans were averaged across the 186 subjects for uptake patterns visualization.

## Experimental design and statistical analyses

*Defining AT and PM networks*

Functional connectivity maps generated in the CN group, with combinations of aH/BA35 versus pH/PHC as seeds, were used to define the AT and PM networks, respectively. In order to highlight brain regions that specifically belong to the AT versus PM systems and to avoid networks overlap, the two sets of 68 connectivity maps were compared using a "paired *t* test" model in the SPM12. A threshold of $P_{\text{voxel(uncorr)}} < 0.01$ with a cluster extent determined by an iterative procedure for estimating cluster-level false-positive rates (Monte Carlo simulation) with 10,000 iterations was used to achieve a cluster corrected statistical significance of $P_{\text{cluster(corr)}} < 0.05$ (AFNI_19.2.26, 3dClustSim program). Note that two separate one sample *t* tests were also performed to evaluate the extent that the networks overlap.

*Structural covariance analyses*

Correlations between summary atrophy rates in BA35 and PHC and voxel-wise atrophy maps in the whole brain were performed in SPM12 to evaluate structural covariance patterns. In order to highlight brain regions that specifically structurally covary with BA35 versus PHC, both BA35 and PHC atrophy rates were entered in a single multiple regression model. A threshold of $P_{\text{voxel(uncorr)}} < 0.01$ with a cluster extent determined by an iterative procedure for estimating cluster-level false-positive rates (Monte Carlo simulation) with 10,000 iterations was used to achieve a corrected statistical significance of $P_{\text{cluster(corr)}} < 0.05$ (AFNI_19.2.26, 3dClustSim program).

*Relationship between structural covariance and functional connectivity*

Three complementary analyses were performed to evaluate the relationship between MTL structural covariance and functional connectivity. First, the spatial overlap between structural covariance patterns (thresholded maps) and the AT and PM networks (thresholded maps) was visually inspected. Then, goodness of fit (GOF) indices between structural

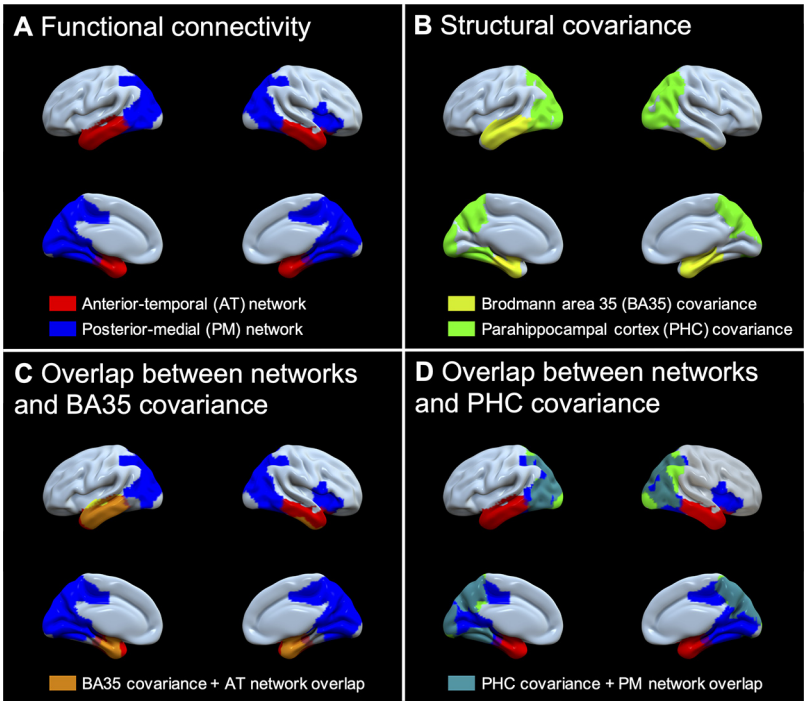


**Figure 3.** Functional connectivity and structural covariance of MTL subregions. ***A***, AT and PM functional networks defined using seed-based correlations (seed: aH and BA35 for AT; pH and PHC for PM) in the CN population from the ABC. Connectivity maps were compared using a paired *t* test ($P_{cluster(corr)} < 0.05$, $P_{voxel(uncorr)} < 0.01$) to highlight specific networks. ***B***, Whole-brain longitudinal structural covariance of BA35 and the PHC cortices ($P_{cluster(corr)} < 0.05$, $P_{voxel(uncorr)} < 0.01$) generated in the ADNI GO/2 population (spanning from A$\beta-$ CN to A$\beta+$ AD patients). ***C***, Overlap between networks and BA35 covariance. ***D***, Overlap between networks and PHC covariance.

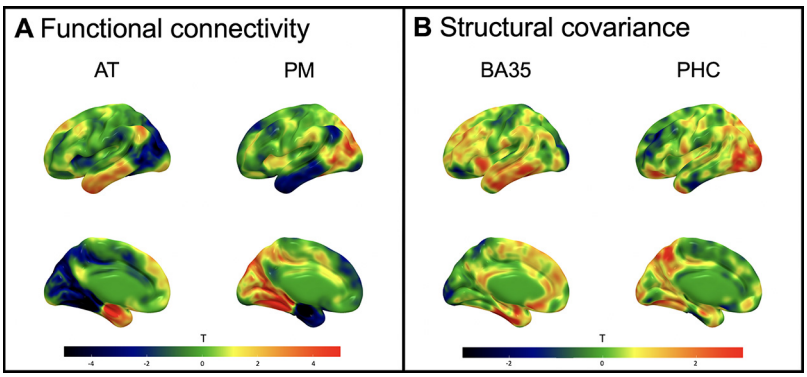


**Figure 4.** Functional connectivity and structural covariance of MTL subregions, continuous *T*-value maps. ***A***, AT and PM functional networks defined using seed-based correlations (seed: aH and BA35 for AT; pH and PHC for PM) in the CN population from the ABC. Connectivity maps were compared using a paired *t* test. ***B***, Whole-brain longitudinal structural covariance of BA35 and the PHC cortices generated in the ADNI GO/2 population (spanning from A$\beta-$ CN to A$\beta+$ AD patients).

covariance maps (nonthresholded T-maps) and AT and PM networks were calculated. GOF is expressed as the difference between the mean T-score of all voxels that fall within the network of interest ($T_{inside}$) and the mean T-score of gray matter voxels outside the network of interest ($T_{outside}$), thus $T_{inside} - T_{outside}$ (Ossenkoppele et al., 2019). Thus, four indices were calculated (two structural covariance maps × two networks). Note that regions corresponding to BA35 and PHC were removed from the network masks to avoid autocorrelation effects. Lastly, correlation analyses were performed between averaged functional connectivity maps (*z* values) and structural covariance maps (*T*-values), for each gray matter voxel ($n = 375{,}222$). A total of four correlation analyses were performed (two structural covariance maps × two averaged functional connectivity maps).

*Vulnerability to AD proteinopathies of the AT and PM networks*

In order to assess the relative vulnerability of the AT versus PM systems to pathologies, masks derived from functional connectivity analyses were used to extract mean SUVR values from amyloid and tau scans, as well as from the tau to amyloid ratio maps. Note that hippocampal ROIs were removed from the AT and PM masks to avoid off target binding contamination from the choroid plexus. For each modality (amyloid, tau, tau to amyloid ratio), a paired *t* test model was employed to compare signal extracted within both networks. In addition, we investigated whether the relationship between amyloid and tau is different within the AT versus the PM networks. This analysis was performed at the voxel level, for each gray matter voxel included in the AT and PM networks. An ANOVA was used with tau SUVR (from the averaged SUVR tau map) as the dependent variable and amyloid SUVR (from the averaged SUVR amyloid map) and network (AT or PM) as the independent variables. The amyloid × network interaction was tested.

## Results

### Defining the AT and PM networks

MTL networks highlighted in the CN population from the ABC dataset are shown in Figure 3*A* (continuous maps are illustrated in Fig. 4). These functional connectivity analyses revealed two distinct networks, corresponding to the AT and PM systems. The AT network, defined by regions more functionally connected to aH/BA35 than pH/PHC, encompasses the amygdala and the temporopolar cortex extending posteriorly to inferior and middle temporal gyri. In contrast, the PM network, defined by regions more functionally connected to pH/PHC than aH/BA35, encompasses the posterior cingulate cortex, the precuneus, the cuneus, the angular and occipital gyri and the right insula. Results from one sample *t* tests are illustrated in Figure 5. The two networks largely overlap, where nonoverlapping regions include the temporal pole for AT and cingulate, occipital and occipitotemporal regions for PM. In addition, analyses were repeated using more stringent thresholds ($P_{voxel(uncorr)} < 0.005$, $P_{cluster(corr)} < 0.05$ and $P_{voxel(uncorr)} < 0.001$, $P_{cluster(corr)} < 0.05$). As illustrated in Figure 6, results were overall unchanged.

### Structural covariance analyses

Longitudinal structural covariance patterns for BA35 and PHC, highlighted in the ADNI GO/2 population (spanning from A$\beta-$ CN to A$\beta+$ AD patients), are shown in Figure 3*B* (continuous maps are illustrated in Fig. 4). Overall, BA35 atrophy covaried with atrophy of the amygdala and the left temporal cortex (just inferior temporal on the right), while PHC atrophy structurally

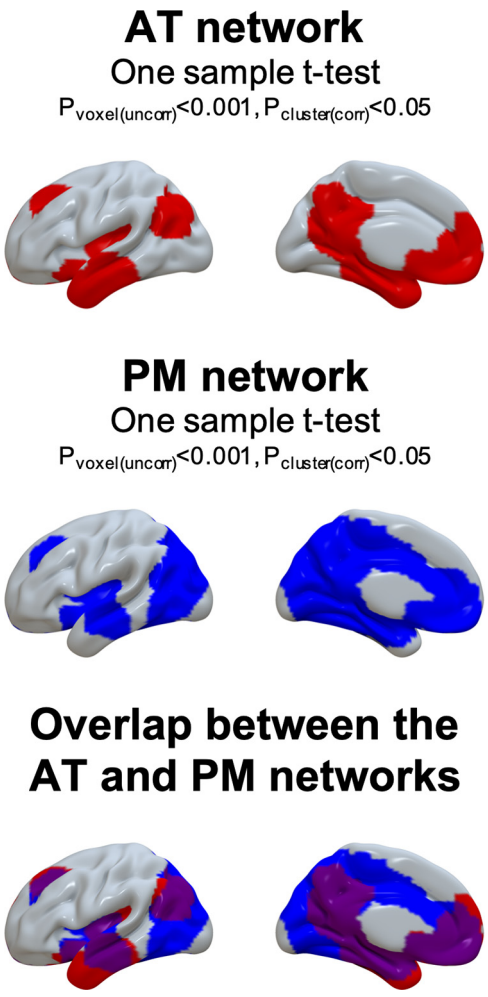


**Figure 5.** AT and PM functional networks defined using two separate one sample *t* tests. The networks were defined using seed-based correlations (seed: aH and BA35 for AT; pH and PHC for PM) in the CN population from the ABC. Two separate one sample *t* tests with a threshold of $P_{voxel(uncorr)} < 0.001$; $P_{cluster(corr)} < 0.05$ were used.

covaried with longitudinal atrophy of the posterior cingulate cortex, the precuneus, the cuneus and the angular and occipital gyri. Analyses were repeated using more stringent thresholds ($P_{voxel(uncorr)} < 0.005$, $P_{cluster(corr)} < 0.05$ and $P_{voxel(uncorr)} < 0.001$, $P_{cluster(corr)} < 0.05$). As illustrated in Figure 6, structural covariance pattern of PHC was overall unchanged. For the structural covariance of BA35, results partially hold using more stringent thresholds, with patterns including the MTL and the posterior portion of the lateral temporal cortex at $P_{voxel(uncorr)} < 0.005$, $P_{cluster(corr)} < 0.05$ while BA35 structurally covaried within the MTL at $P_{voxel(uncorr)} < 0.001$, $P_{cluster(corr)} < 0.05$.

### Relationship between structural covariance and functional connectivity

The relationship between MTL structural covariance and functional connectivity was assessed using three different and complementary approaches. First, the spatial overlap between structural covariance patterns and the AT and PM networks is illustrated in Figure 3*C*,*D*. Overall, BA35 structural covariance overlapped with the AT network while PHC structural covariance overlapped with the PM network with little structural covariance outside of the respective networks. Note that the same conclusion applies when networks derived from one sample *t* tests are considered. Second, we generated GOF indices between structural covariance maps and AT and PM networks. BA35 covariance showed better GOF with the AT system (1.10 vs −0.50 for PM). In contrast, PHC covariance showed better GOF with the PM system (0.92 vs −0.33 for AT). Third, each voxel of the averaged connectivity maps generated in the CN population from the ABC were correlated with each voxel of structural covariance maps generated in the ADNI GO/2 population. As illustrated in Figure 7, BA35 structural covariance demonstrated better correlation with AT functional connectivity ($r = 0.24$, $p < 0.001$ vs $r = 0.04$, $p < 0.001$ for PM functional connectivity), while PHC structural covariance displayed better correlation with PM functional connectivity ($r = 0.18$, $p < 0.001$ vs $r = -0.03$, $p < 0.001$ for AT functional connectivity). To confirm these observations, correlation coefficients were statistically compared using the R package "cocor" (Diedenhofen and Musch, 2015). As reported in Table 2, the results of all tests lead to the convergent conclusion that BA35 structural covariance is significantly more associated with AT functional connectivity than PM functional connectivity, while PHC structural covariance is significantly more associated with PM functional connectivity than AT functional connectivity.

### Vulnerability to AD proteinopathies of the AT and PM networks

Average uptake patterns for tau, amyloid and tau/amyloid PET are illustrated in Figure 8. Overall, tau PET uptake was particularly high in temporal (medial and lateral), parietal (medial and inferior) and orbitofrontal regions, while amyloid uptake was more diffuse and involved almost all brain regions (except the MTL). Tau/amyloid signal was high in temporal regions, particularly in the MTL, as well as in the lateral parietal cortex. Note that the signal was relatively low in midline parietal structures. When comparing signal within the AT versus PM systems (Fig. 8), tau uptake was significantly higher in the AT network than in the PM network ($t_{(185)} = 3.52$, $p = 5.40e^{-04}$), while amyloid uptake was higher in the PM network than in the AT network ($t_{(185)} = -30.25$, $p < 2.2e^{-16}$). Tau/amyloid signal was significantly higher in the AT network than in the PM network ($t_{(185)} = 18.08$, $p < 2.2e^{-16}$). These analyses were repeated by including additional 195 A$\beta$− CN individuals. Results were unchanged, although more significant, with higher tau uptake and tau/amyloid ratio in AT than in PM ($t_{(380)} = 4.91$, $p = 1.36e^{-06}$; $t_{(380)} = 32.37$, $p < 2.2e^{-16}$, respectively) and higher amyloid uptake in PM than in AT ($t_{(380)} = -45.47$, $p < 2.2e^{-16}$). Lastly, the analysis performed at the voxel level showed a significant interaction of the effects of amyloid and network on tau ($F_{(1,116663)} = 6224.3$, $p < 2.2e^{-16}$). As illustrated in Figure 9, the slope of the association between tau and amyloid SUVRs was steeper within the AT network than in the PM network.

## Discussion

The aim of the present study was to evaluate the structural and molecular vulnerabilities of two specific MTL networks, namely, the AT and PM networks, over the course of AD. In particular, we aimed to determine whether these networks displayed evidence of dissociable neurodegenerative change and the degree to which they differed in underlying molecular pathology, which would have implications for the pathophysiologic cascade of AD and the relative vulnerability of these networks. To that end, we used a combination of rs-fMRI, longitudinal structural MRI, as

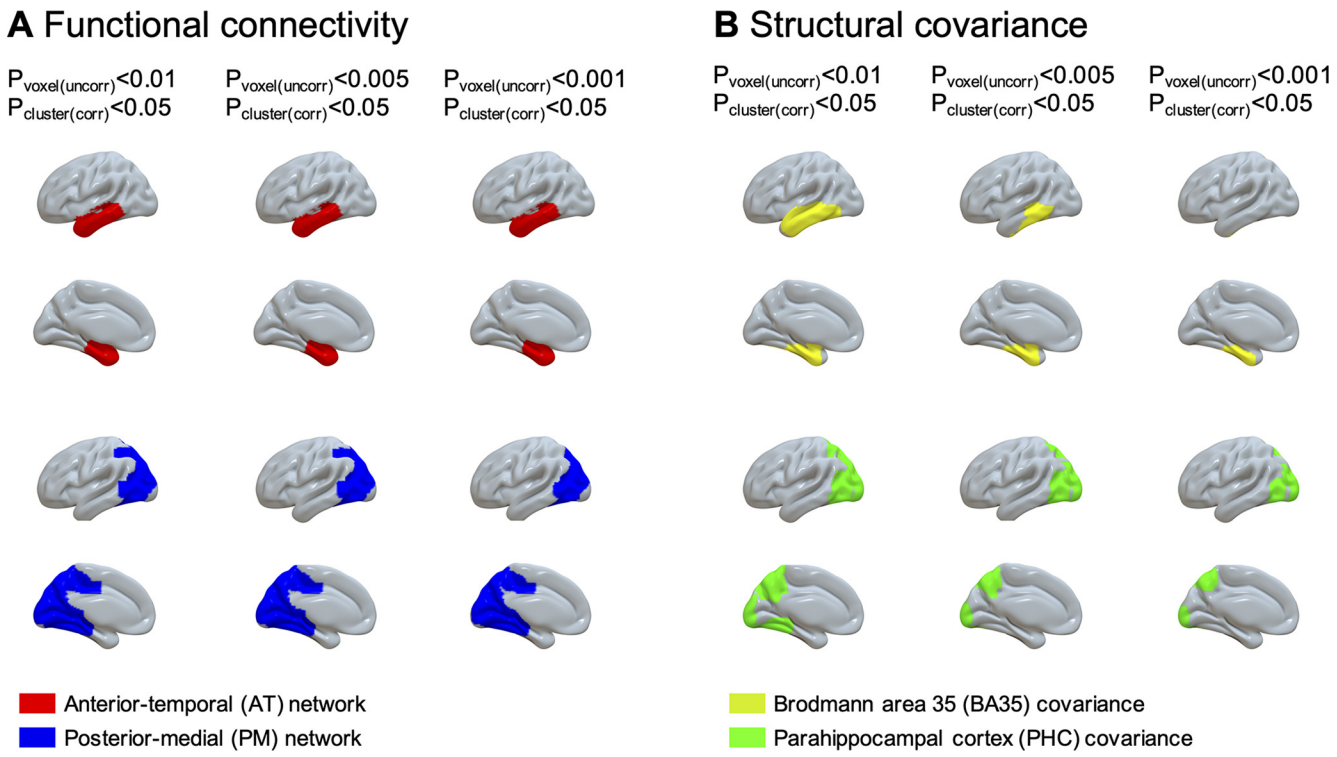


**Figure 6.** Functional connectivity and structural covariance of MTL subregions using different thresholds. ***A***, AT and PM functional networks defined using seed-based correlations (seed: aH and BA35 for AT; pH and PHC for PM) in the CN population from the ABC. Connectivity maps were compared using a paired *t* test ($P_{cluster(corr)} < 0.05$, $P_{voxel(uncorr)} < 0.01/P_{cluster(corr)} < 0.05$, $P_{voxel(uncorr)} < 0.005/P_{cluster(corr)} < 0.05$, $P_{voxel(uncorr)} < 0.001$) to highlight specific networks. ***B***, Whole-brain longitudinal structural covariance of BA35 and the PHC cortices ($P_{cluster(corr)} < 0.05$, $P_{voxel(uncorr)} < 0.01/P_{cluster(corr)} < 0.05$, $P_{voxel(uncorr)} < 0.005/P_{cluster(corr)} < 0.05$, $P_{voxel(uncorr)} < 0.001$) generated in the ADNI GO/2 population (spanning from A$\beta-$ CN to A$\beta+$ AD patients).

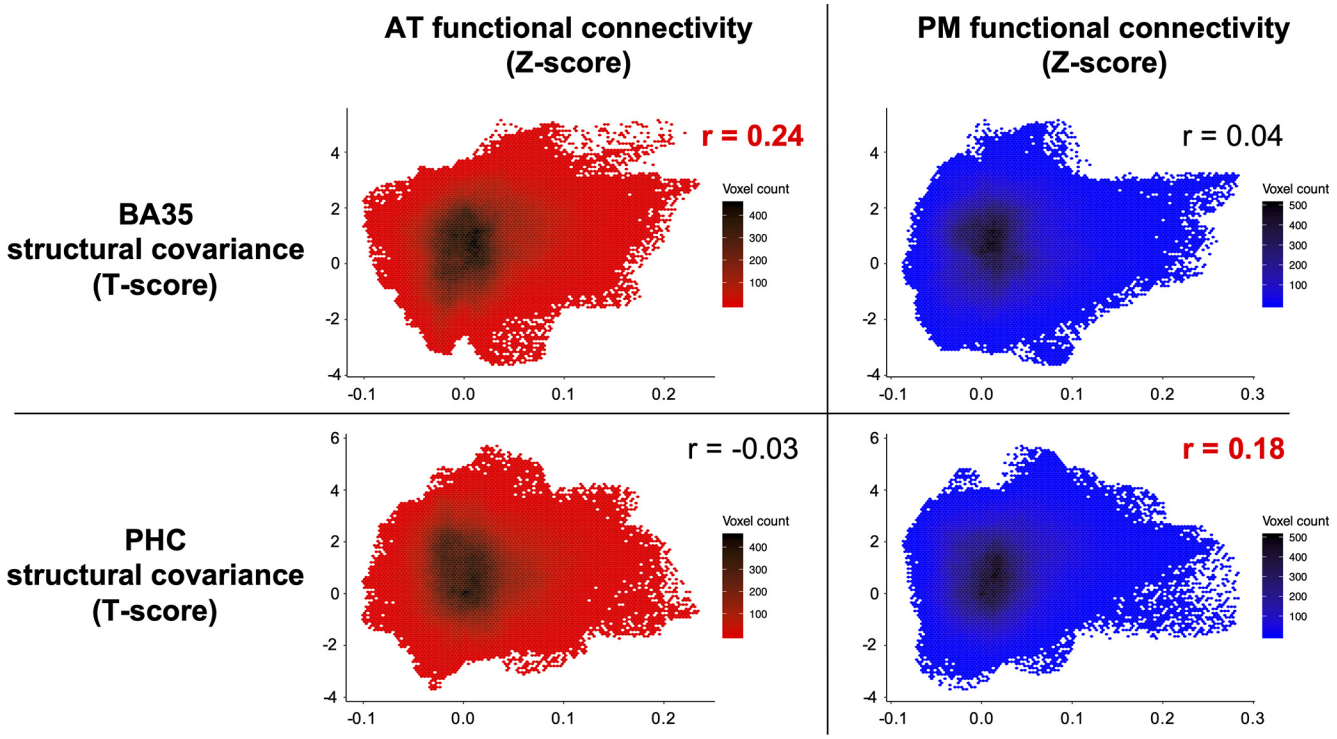


**Figure 7.** Correlations between functional connectivity and structural covariance. Each voxel of the averaged connectivity maps (*z* values) generated in the CN population from the ABC were correlated with each voxel of structural covariance maps (*T*-values) generated in the ADNI GO/2 population.

**Table 2. Correlation coefficients comparisons**

| | BA35 structural covariance ~ AT functional connectivity vs BA35 structural covariance ~ PM functional connectivity | PHC structural covariance ~ AT functional connectivity vs PHC structural covariance ~ PM functional connectivity |
|---|---|---|
| Pearson and Filon's z (1898) | z = 144.0206, *p*-value = 0.0000 | z = −150.4716, *p*-value = 0.0000 |
| Hotelling's t (1940) | *t* = 146.3813, df = 375219, *p*-value = 0.0000 | *t* = −152.9268, df = 375219, *p*-value = 0.0000 |
| Williams' t (1959) | *t* = 146.3212, df = 375219, *p*-value = 0.0000 | *t* = −152.9084, df = 375219, *p*-value = 0.0000 |
| Olkin's z (1967) | z = 144.0206, *p*-value = 0.0000 | z = −150.4716, *p*-value = 0.0000 |
| Dunn and Clark's z (1969) | z = 143.3883, *p*-value = 0.0000 | z = −149.5178, *p*-value = 0.0000 |
| Stanley and Hills' (1970) | *t* = 146.3813, df = 375219, *p*-value = 0.0000 | *t* = −152.9268, df = 375219, *p*-value = 0.0000 |
| Steiger's (1980) | z = 142.8124, *p*-value = 0.0000 | z = −148.8888, *p*-value = 0.0000 |
| Meng, Rosenthal, and Rubin's z (1992) | z = 142.2512, *p*-value = 0.0000 | z = −148.2490, *p*-value = 0.0000 |
| Hittner, May, and Silver's (2003) | z = 142.7896, *p*-value = 0.0000 | z = −148.8813, *p*-value = 0.0000 |
| Zou's (2007) confidence interval | 0.1914 0.1967 | −0.2066 −0.2013 |

Statistical comparisons were performed using the R package "cocor" (Diedenhofen and Musch, 2015).

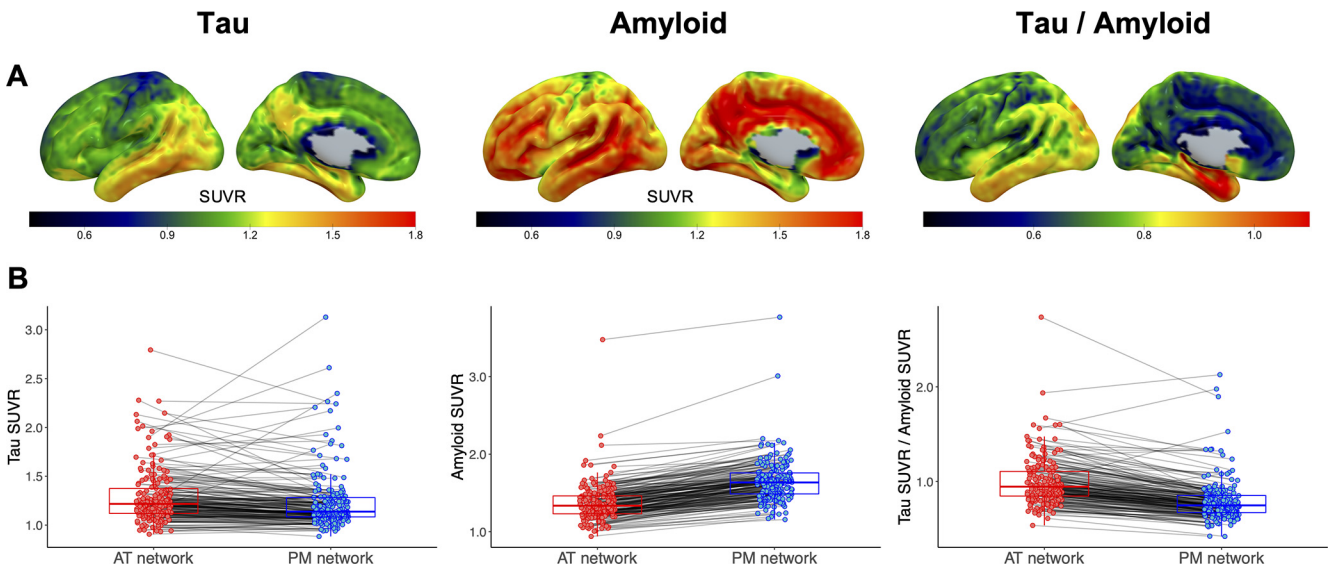


**Figure 8.** Tau and amyloid accumulation within the AT and PM networks. ***A***, Tau, amyloid, and tau/amyloid ratio scans were averaged across 186 subjects for uptake patterns visualization. ***B***, Mean SUVR values in the AT and PM networks were estimated from amyloid, tau, and tau/amyloid ratio maps. For each modality, a paired *t* test model was used to compare signal extracted within both networks.

well as tau and amyloid PET data acquired in three distinct cohorts covering the full AD spectrum.

Consistent with prior literature, our functional connectivity analyses performed in a group of 68 CN individuals revealed two specific MTL networks. Overall, the amygdala and the temporopolar cortex (extending posteriorly to inferior and middle temporal gyri) were more functionally connected to a seed composed of the aH and BA35 than the pH and PHC. In contrast, the posterior cingulate cortex, the precuneus, the cuneus, the angular and occipital gyri and the right insula were more functionally connected to pH/PHC than aH/BA35. As expected, these specific networks are overall in line with the two systems proposed by Ranganath and Ritchey (2012) in their review based on anatomic and functional studies performed in humans, monkeys and rats. Recently, the AT and PM networks have been investigated *in vivo* in humans using neuroimaging techniques. Studies have consistently reported two distinct MTL systems, although subtle differences can be noticed, likely because different approaches were employed. For example, the AT and PM networks were highlighted using seeds made of PRC versus PHC (Kahn et al., 2008; Libby et al., 2012; Zhuo et al., 2016), aH versus pH (La Joie et al., 2014; Das et al., 2015; Vogel et al., 2020), or anterolateral ERC versus posteromedial ERC (Adams et al., 2019). To our knowledge, the present study is the first to use combinations of hippocampal and extrahippocampal regions (aH/BA35 vs pH/PHC) as seeds. Note that it might appear more appropriate to use BA35 alone as a seed to parallel the structural covariance analyses. However, as illustrated in Figure 10, a subpart of the AT network was obtained, since BA35 is only a portion of PRC. Further, BA35 is a very small region located in a part of the brain which is prone to distortion in fMRI scans, and might not be ideal to be used as a seed by itself. Thus, combining MTL nodes belonging to the same network appeared as a reasonable approach and allowed to highlight specific networks corresponding to the AT and PM systems.

Using longitudinal structural MRI data in a large population from ADNI GO/2 covering the AD spectrum from CN to mild AD-related dementia, our analyses revealed distinct MTL structural covariance patterns. BA35 atrophy covaried with atrophy of the amygdala and the left temporal cortex, while PHC atrophy structurally covaried with longitudinal atrophy of the posterior cingulate cortex, the precuneus, the cuneus and the angular and occipital gyri. Over the past few years, several studies have been performed to evaluate MTL structural covariance with the rest of the brain in the context of normal and pathologic aging (Bohbot et al., 2007; Olman et al., 2009; Persson et al., 2014;

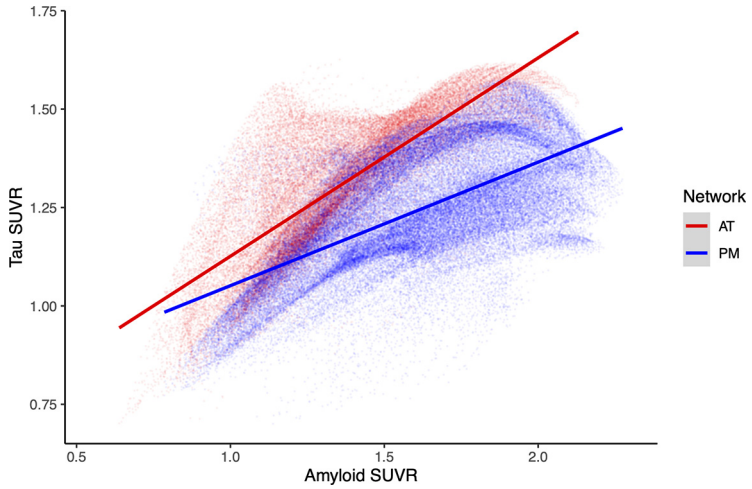


**Figure 9.** Association between tau and amyloid within the AT versus PM networks. Each gray matter voxels from the averaged SUVR tau and amyloid maps and included in the AT and PM masks ($n = 116{,}667$) were used to investigated whether the relationship between amyloid and tau is different within the AT versus the PM networks.

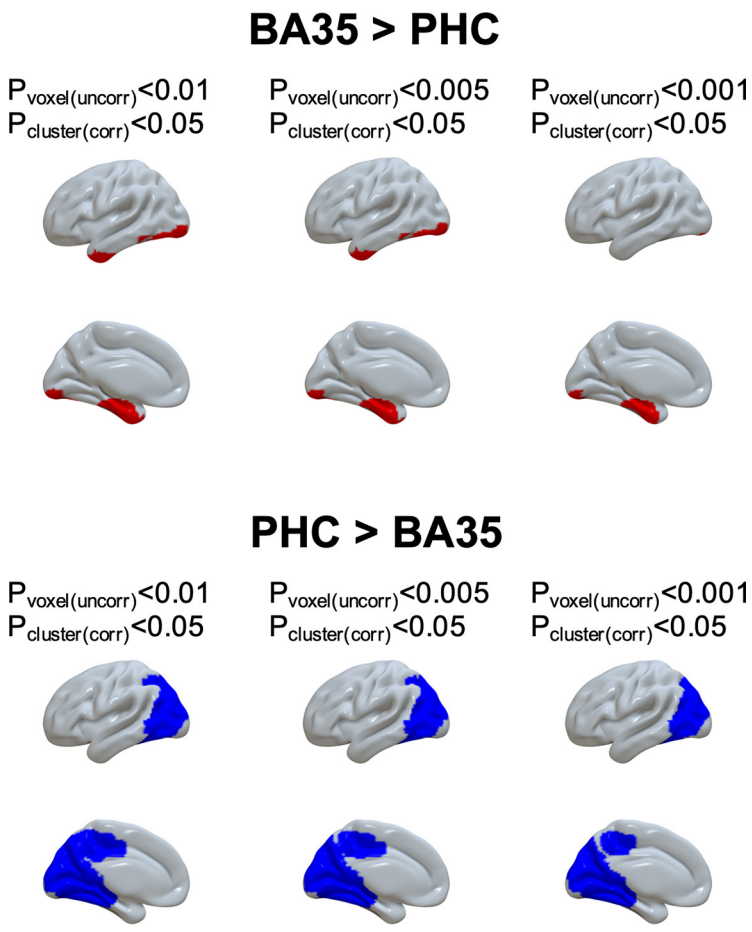


**Figure 10.** Functional connectivity of MTL subregions, alternative seeds. AT and PM functional networks defined using seed-based correlations (seed: BA35 for AT; PHC for PM) in the CN population from the ABC. Connectivity maps were compared using a paired *t* test ($P_{cluster(corr)} < 0.05$, $P_{voxel(uncorr)} < 0.01/P_{cluster(corr)} < 0.05$, $P_{voxel(uncorr)} < 0.005/P_{cluster(corr)} < 0.05$, $P_{voxel(uncorr)} < 0.001$) to highlight specific networks.

Montembeault et al., 2016; Stening et al., 2017; Chang et al., 2018; Li et al., 2018, 2019; Nordin et al., 2018; Wang et al., 2018; Plachti et al., 2020; Vogel et al., 2020). Previous investigations demonstrated that structural covariance differs across the longitudinal axis of the hippocampus, with aH overall covarying with temporal areas while pH covaried with parietal and occipital regions (Persson et al., 2014; Stening et al., 2017; Nordin et al., 2018; Li et al., 2019; Vogel et al., 2020). These results are consistent with our observations. However, it is important to note that these previous works were performed using cross-sectional data only, while our analyses were based on a longitudinal design, which is a more suitable approach to evaluate more pure effects of active neurodegeneration and disease progression topography, given that cross-sectional analyses may be influenced by developmental covariance. In addition, the present study is the first, to our knowledge, to contrast the structural covariance of two extrahippocampal regions (BA35 and PHC) across the AD spectrum. Importantly, BA35 and PHC structural covariance patterns overlapped with the AT and PM networks, respectively, supporting the notion that not only are these regions important nodes of functionally dissociable networks, but that neurodegeneration occurs in a dissociable fashion between them in the context of AD. Our analyses also revealed specific correlations between structural covariance and functional connectivity. These observations are in line with several neuroimaging works showing a relationship between functional connectivity and tau/neurodegeneration topography and propagation (Seeley et al., 2009; Zhou et al., 2012; Mutlu et al., 2017; Bischof et al., 2019; Ossenkoppele et al., 2019; Franzmeier et al., 2020a,b). Altogether, these observations performed *in vivo* in humans support the "prion-like" propagation theory which proposed that AD pathology, more particularly tau pathology and subsequent atrophy, spreads across anatomically interconnected brain regions (Brettschneider et al., 2015; Peng et al., 2020). In addition, the MTL structural covariance patterns highlighted here overall recapitulate the global AD atrophy pattern, classically described in the literature, where temporal and parietal regions are among the most affected brain areas (Dickerson et al., 2009; La Joie et al., 2012; Pini et al., 2016). This strengthens the view that the MTL is an epicenter of AD neurodegeneration but also suggests that pathology propagates to the neocortex through two distinct networks.

Lastly, we used PET data from ADNI 3, acquired in A$\beta$+ CN, MCI and AD patients, to evaluate the relative vulnerability of the AT and PM networks to amyloid and tau pathologies. Our analyses showed that tau uptake was relatively higher in the AT network than in the PM network, while amyloid uptake was

relatively higher in the PM network than in the AT network. Similar to tau uptake, tau to amyloid ratio signal was more prominent in the AT network than in the PM network. Note that this ratio signal was particularly high in the MTL, suggesting that tau pathology in this region is relatively independent of amyloid. In addition, we found a significant amyloid × network interaction, where the slope of the association between tau and amyloid SUVRs was steeper within the AT network than in the PM network. This indicates that for a given level of amyloid, tau level is higher in AT than in PM. These results may suggest that more of the tau in the PM system is associated with neuritic tau given the higher amyloid plaque burden while we might expect more tangles in the absence of neuritic plaques in AT. However, this hypothesis is purely speculative. While tau levels are lower in the PM network, there is still significant tau pathology present in these regions, at least in the majority of patients studied here. Lastly, local relationships between amyloid and tau were explored in the present study, but nonlocal interactions between the two pathologies may also exist.

Overall, our observations are consistent with recent reports investigating AD pathology within MTL networks (Adams et al., 2019; Maass et al., 2019). More precisely, Adams et al. (2019) showed that in CN older adults, tau pathology is preferentially deposited in regions that are functionally connected to the anterolateral ERC (i.e., the AT system), with stronger connectivity being associated with increased tau deposition. Maass et al. (2019) also described early tau deposition in the AT system, which was associated with deficits in mnemonic object discrimination, while the presence of amyloid deposits was preferentially found in PM regions. Thus, early AD pathology seems to target both systems and might explain the functional disruptions observed in patients in previous investigations (Das et al., 2015; Chen et al., 2016; Liu et al., 2016; Berron et al., 2020), but does so with differential pathologic underpinnings. Altogether, these data suggest a predominant role of the AT and PM networks in the pathophysiology of AD.

Our study has some limitations. We used data from three different datasets: resting-state functional connectivity data were acquired at University of Pennsylvania, longitudinal structural MRI data came from ADNI GO/2, and amyloid and tau PET data came from ADNI 3. Thereby, we could not assess the direct relationships between functional connectivity, the presence of pathologies and structural covariance. Having all such data acquired in the same participants would have allowed us to explore pathologic mechanisms more deeply. However, this can also be seen as a strength, since this indicates that our results are potentially generalizable. Further studies performed on a unique sample (with longitudinal imaging in all modalities) and including more advanced patients are thus needed to fully understand the involvement of the AT and PM networks in the pathophysiology of AD across the disease spectrum.

## References


Adams JN, Maass A, Harrison TM, Baker SL, Jagust WJ (2019) Cortical tau deposition follows patterns of entorhinal functional connectivity in aging. Elife 8:e49132.

Avants BB, Tustison NJ, Wu J, Cook PA, Gee JC (2011) An open source multivariate framework for n-tissue segmentation with evaluation on public data. Neuroinform 9:381–400.

Berron D, van Westen D, Ossenkoppele R, Strandberg O, Hansson O (2020) Medial temporal lobe connectivity and its associations with cognition in early Alzheimer's disease. Brain 143:1233–1248.

Bischof GN, Ewers M, Franzmeier N, Grothe MJ, Hoenig M, Kocagoncu E, Neitzel J, Rowe JB, Strafella A, Drzezga A, van Eimeren T; MINC faculty (2019) Connectomics and molecular imaging in neurodegeneration. Eur J Nucl Med Mol Imaging 46:2819–2830.

Bohbot VD, Lerch J, Thorndycraft B, Iaria G, Zijdenbos AP (2007) Gray matter differences correlate with spontaneous strategies in a human virtual navigation task. J Neurosci 27:10078–10083.

Braak H, Braak E (1991) Neuropathological stageing of Alzheimer-related changes. Acta Neuropathol 82:239–259.

Brettschneider J, Del Tredici K, Lee VMY, Trojanowski JQ (2015) Spreading of pathology in neurodegenerative diseases: a focus on human studies. Nat Rev Neurosci 16:109–120.

Chang YT, Huang CW, Chang WN, Lee JJ, Chang CC (2018) Altered functional network affects amyloid and structural covariance in Alzheimer's disease. Biomed Res Int 2018:8565620.

Chen J, Duan X, Shu H, Wang Z, Long Z, Liu D, Liao W, Shi Y, Chen H, Zhang Z (2016) Differential contributions of subregions of medial temporal lobe to memory system in amnestic mild cognitive impairment: insights from fMRI study. Sci Rep 6:26148.

Das SR, Pluta J, Mancuso L, Kliot D, Yushkevich PA, Wolk DA (2015) Anterior and posterior MTL networks in aging and MCI. Neurobiology of Aging 36:S141–S150.e1.

Das SR, Xie L, Wisse LEM, Ittyerah R, Tustison NJ, Dickerson BC, Yushkevich PA, Wolk DA; Alzheimer's Disease Neuroimaging Initiative (2018) Longitudinal and cross-sectional structural magnetic resonance imaging correlates of AV-1451 uptake. Neurobiol Aging 66:49–58.

de Flores R, Wisse LEM, Das SR, Xie L, McMillan CT, Trojanowski JQ, Robinson JL, Grossman M, Lee E, Irwin DJ, Yushkevich PA, Wolk DA (2020) Contribution of mixed pathology to medial temporal lobe atrophy in Alzheimer's disease. Alzheimers Dement 16:843–852.

de Souza LC, Chupin M, Lamari F, Jardel C, Leclercq D, Colliot O, Lehéricy S, Dubois B, Sarazin M (2012) CSF tau markers are correlated with hippocampal volume in Alzheimer's disease. Neurobiol Aging 33:1253–1257.

Dickerson BC, Bakkour A, Salat DH, Feczko E, Pacheco J, Greve DN, Grodstein F, Wright CI, Blacker D, Rosas HD, Sperling RA, Atri A, Growdon JH, Hyman BT, Morris JC, Fischl B, Buckner RL (2009) The cortical signature of Alzheimer's disease: regionally specific cortical thinning relates to symptom severity in very mild to mild AD dementia and is detectable in asymptomatic amyloid-positive individuals. Cereb Cortex 19:497–510.

Diedenhofen B, Musch J (2015) cocor: a comprehensive solution for the statistical comparison of correlations. PLoS One 10:e0121945.

Franzmeier N, Neitzel J, Rubinski A, Smith R, Strandberg O, Ossenkoppele R, Hansson O, Ewers M; Alzheimer's Disease Neuroimaging Initiative (ADNI) (2020a) Functional brain architecture is associated with the rate of tau accumulation in Alzheimer's disease. Nat Commun 11:17.

Franzmeier N, Dewenter A, Frontzkowski L, Dichgans M, Rubinski A, Neitzel J, Smith R, Strandberg O, Ossenkoppele R, Buerger K, Duering M, Hansson O, Ewers M (2020b) Patient-centered connectivity-based prediction of tau pathology spread in Alzheimer's disease. Sci Adv 6:eabd1327.

Friston KJ, Frith CD, Frackowiak RS, Turner R (1995) Characterizing dynamic brain responses with fMRI: a multivariate approach. Neuroimage 2:166–172.

Jack CR, Bernstein MA, Fox NC, Thompson P, Alexander G, Harvey D, Borowski B, Britson PJ, L Whitwell J, Ward C, Dale AM, Felmlee JP, Gunter JL, Hill DLG, Killiany R, Schuff N, Fox-Bosetti S, Lin C, Studholme C, DeCarli CS, et al. (2008) The Alzheimer's disease neuroimaging initiative (ADNI): MRI methods. J Magn Reson Imaging 27:685–691.

Jellinger KA (2020) Neuropathological assessment of the Alzheimer spectrum. J Neural Transm (Vienna) 127:1229–1256.

La Joie R, Perrotin A, Barré L, Hommet C, Mézenge F, Ibazizene M, Camus V, Abbas A, Landeau B, Guilloteau D, de La Sayette V, Eustache F, Desgranges B, Chételat G (2012) Region-specific hierarchy between atrophy, hypometabolism, and $\beta$-amyloid ($A\beta$) load in Alzheimer's disease dementia. J Neurosci 32:16265–16273.

La Joie R, Landeau B, Perrotin A, Bejanin A, Egret S, Pélerin A, Mézenge F, Belliard S, de La Sayette V, Eustache F, Desgranges B, Chételat G (2014) Intrinsic connectivity identifies the hippocampus as a main crossroad between Alzheimer's and semantic dementia-targeted networks. Neuron 81:1417–1428.

La Joie R, Visani AV, Baker SL, Brown JA, Bourakova V, Cha J, Chaudhary K, Edwards L, Iaccarino L, Janabi M, Lesman-Segev OH, Miller ZA, Perry DC, O'Neil JP, Pham J, Rojas JC, Rosen HJ, Seeley WW, Tsai RM, Miller BL, et al. (2020) Prospective longitudinal atrophy in Alzheimer's disease correlates with the intensity and topography of baseline tau-PET. Sci Transl Med 12:1–13.

Kahn I, Andrews-Hanna JR, Vincent JL, Snyder AZ, Buckner RL (2008) Distinct cortical anatomy linked to subregions of the medial temporal lobe revealed by intrinsic functional connectivity. J Neurophysiol 100:129–139.

Landau SM, Breault C, Joshi AD, Pontecorvo M, Mathis CA, Jagust WJ, Mintun MA; Alzheimer's Disease Neuroimaging Initiative (2013) Amyloid-$\beta$ imaging with Pittsburgh compound B and Florbetapir: comparing radiotracers and quantification methods. J Nucl Med 54:70–77.

Landman BA, Warfield SK (2012) MICCAI 2012 workshop on multi-atlas labeling. Available at http://www.neuromorphometrics.com/2012_MICCAI_Challenge_Data.html. Accessed November 30, 2020.

Leow AD, Klunder AD, Jack CR, Toga AW, Dale AM, Bernstein MA, Britson PJ, Gunter JL, Ward CP, Whitwell JL, Borowski BJ, Fleisher AS, Fox NC, Harvey D, Kornak J, Schuff N, Studholme C, Alexander GE, Weiner MW, Thompson PM; ADNI Preparatory Phase Study (2006) Longitudinal stability of MRI for mapping brain change using tensor-based morphometry. Neuroimage 31:627–640.

Li K, Luo X, Zeng Q, Huang P, Shen Z, Xu X, Xu J, Wang C, Zhou J, Zhang M; Alzheimer's Disease Neuroimaging Initiative (2019) Gray matter structural covariance networks changes along the Alzheimer's disease continuum. Neuroimage Clin 23:101828.

Li X, Li Q, Wang X, Li D, Li S (2018) Differential age-related changes in structural covariance networks of human anterior and posterior hippocampus. Front Physiol 9:518.

Libby LA, Ekstrom AD, Ragland JD, Ranganath C (2012) Differential connectivity of perirhinal and parahippocampal cortices within human hippocampal subregions revealed by high-resolution functional imaging. J Neurosci 32:6550–6560.

Liu J, Zhang X, Yu C, Duan Y, Zhuo J, Cui Y, Liu B, Li K, Jiang T, Liu Y (2016) Impaired parahippocampus connectivity in mild cognitive impairment and Alzheimer's disease. J Alzheimers Dis 49:1051–1064.

Maass A, Berron D, Libby LA, Ranganath C, Düzel E (2015) Functional subregions of the human entorhinal cortex. Elife 4:e06426.

Maass A, Berron D, Harrison TM, Adams JN, La Joie R, Baker S, Mellinger T, Bell RK, Swinnerton K, Inglis B, Rabinovici GD, Düzel E, Jagust WJ (2019) Alzheimer's pathology targets distinct memory networks in the ageing brain. Brain 142:2492–2509.

Montembeault M, Rouleau I, Provost JS, Brambati SM; Alzheimer's Disease Neuroimaging Initiative (2016) Altered gray matter structural covariance networks in early stages of Alzheimer's disease. Cereb Cortex 26:2650–2662.

Mutlu J, Landeau B, Gaubert M, de La Sayette V, Desgranges B, Chételat G (2017) Distinct influence of specific versus global connectivity on the different Alzheimer's disease biomarkers. Brain 140:3317–3328.

Nordin K, Persson J, Stening E, Herlitz A, Larsson E-M, Söderlund H (2018) Structural whole-brain covariance of the anterior and posterior hippocampus: associations with age and memory. Hippocampus 28:151–163.

Olman CA, Davachi L, Inati S (2009) Distortion and signal loss in medial temporal lobe. PLoS One 4:e8160.

Ossenkoppele R, Iaccarino L, Schonhaut DR, Brown JA, La Joie R, O'Neil JP, Janabi M, Baker SL, Kramer JH, Gorno-Tempini M-L, Miller BL, Rosen HJ, Seeley WW, Jagust WJ, Rabinovici GD (2019) Tau covariance patterns in Alzheimer's disease patients match intrinsic connectivity networks in the healthy brain. Neuroimage Clin 23:101848.

Peng C, Trojanowski JQ, Lee VMY (2020) Protein transmission in neurodegenerative disease. Nat Rev Neurol 16:199–212.

Persson J, Spreng RN, Turner G, Herlitz A, Morell A, Stening E, Wahlund L-O, Wikström J, Söderlund H (2014) Sex differences in volume and structural covariance of the anterior and posterior hippocampus. Neuroimage 99:215–225.

Pini L, Pievani M, Bocchetta M, Altomare D, Bosco P, Cavedo E, Galluzzi S, Marizzoni M, Frisoni GB (2016) Brain atrophy in Alzheimer's disease and aging. Ageing Res Rev 30:25–24.

Plachti A, Kharabian S, Eickhoff SB, Maleki Balajoo S, Hoffstaedter F, Varikuti DP, Jockwitz C, Caspers S, Amunts K, Genon S (2020) Hippocampus co-atrophy pattern in dementia deviates from covariance patterns across the lifespan. Brain 143:2788–2802.

Ranganath C, Ritchey M (2012) Two cortical systems for memory-guided behaviour. Nat Rev Neurosci 13:713–726.

Salami A, Wåhlin A, Kaboodvand N, Lundquist A, Nyberg L (2016) Longitudinal evidence for dissociation of anterior and posterior MTL resting-state connectivity in aging: links to perfusion and memory. Cereb Cortex 26:3953–3963.

Seeley WW, Crawford RK, Zhou J, Miller BL, Greicius MD (2009) Neurodegenerative diseases target large-scale human brain networks. Neuron 62:42–52.

Stening E, Persson J, Eriksson E, Wahlund LO, Zetterberg H, Söderlund H (2017) Specific patterns of whole-brain structural covariance of the anterior and posterior hippocampus in young APOE $\varepsilon$4 carriers. Behav Brain Res 326:256–264.

Tardif CL, Devenyi GA, Amaral RSC, Pelleieux S, Poirier J, Rosa-Neto P, Breitner J, Chakravarty MM; PREVENT-AD Research Group (2018) Regionally specific changes in the hippocampal circuitry accompany progression of cerebrospinal fluid biomarkers in preclinical Alzheimer's disease. Hum Brain Mapp 39:971–984.

Tustison NJ, Cook PA, Klein A, Song G, Das SR, Duda JT, Kandel BM, van Strien N, Stone JR, Gee JC, Avants BB (2014) Large-scale evaluation of ANTs and FreeSurfer cortical thickness measurements. Neuroimage 99:166–179.

Tustison NJ, Holbrook AJ, Avants BB, Roberts JM, Cook PA, Reagh ZM, Duda JT, Stone JR, Gillen DL, Yassa MA; Alzheimer's Disease Neuroimaging Initiative (2019) Longitudinal mapping of cortical thickness measurements: an Alzheimer's disease neuroimaging initiative-based evaluation study. J Alzheimers Dis 71:165–183.

Vogel JW, La Joie R, Grothe MJ, Diaz-Papkovich A, Doyle A, Vachon-Presseau E, Lepage C, Vos de Wael R, Thomas RA, Iturria-Medina Y, Bernhardt B, Rabinovici GD, Evans AC (2020) A molecular gradient along the longitudinal axis of the human hippocampus informs large-scale behavioral systems. Nat Commun 11:960.

Wang H, Suh JW, Das S, Pluta J, Altinay M, Yushkevich P (2011) Regression-based label fusion for multi-atlas segmentation. Conf Comput Vis Pattern Recognit Workshops, pp 1113–1120. doi: 10.1109/CVPR.2011.5995382.

Wang X, Yu Y, Zhao W, Li Q, Li X, Li S, Yin C, Han Y (2018) Altered whole-brain structural covariance of the hippocampal subfields in subcortical vascular mild cognitive impairment and amnestic mild cognitive impairment patients. Front Neurol 9:342.

Weintraub S, Besser L, Dodge HH, Teylan M, Ferris S, Goldstein FC, Giordani B, Kramer J, Loewenstein D, Marson D, Mungas D, Salmon D, Welsh-Bohmer K, Zhou XH, Shirk SD, Atri A, Kukull WA, Phelps C, Morris JC (2018) Version 3 of the Alzheimer disease centers' neuropsychological test battery in the uniform data set (UDS). Alzheimer Dis Assoc Disord 32:10–17.

Whitwell JL, Josephs KA, Murray ME, Kantarci K, Przybelski SA, Weigand SD, Vemuri P, Senjem ML, Parisi JE, Knopman DS, Boeve BF, Petersen RC, Dickson DW, Jack CR (2008) MRI correlates of neurofibrillary tangle pathology at autopsy: a voxel-based morphometry study. Neurology 71:743–749.

Xie L, Das SR, Wisse LEM, Ittyerah R, Yushkevich PA, Wolk DA; Alzheimer's Disease Neuroimaging Initiative (2018) Early tau burden correlates with higher rate of atrophy in transentorhinal cortex. J Alzheimers Dis 62:85–92.

Xie L, Wisse LEM, Pluta J, de Flores R, Piskin V, Manjón JV, Wang H, Das SR, Ding SL, Wolk DA, Yushkevich PA; Alzheimer's Disease Neuroimaging Initiative (2019) Automated segmentation of medial temporal lobe subregions on in vivo T1-weighted MRI in early stages of Alzheimer's disease. Hum Brain Mapp 40:3431–3451.

Xie L, Wisse LEM, Das SR, Vergnet N, Dong M, Ittyerah R, Flores R, Yushkevich PA, Wolk DA; Alzheimer's Disease Neuroimaging Initiative (2020) Longitudinal atrophy in early Braak regions in preclinical Alzheimer's disease. Hum Brain Mapp 41:4704–4717.

Zhou J, Gennatas ED, Kramer JH, Miller BL, Seeley WW (2012) Predicting regional neurodegeneration from the healthy brain functional connectome. Neuron 73:1216–1227.

Zhuo J, Fan L, Liu Y, Zhang Y, Yu C, Jiang T (2016) Connectivity profiles reveal a transition subarea in the parahippocampal region that integrates the anterior temporal-posterior medial systems. J Neurosci 36:2782–2795.